Purkinje Cell Loss in Experimental Autoimmune Encephalomyelitis

Allan MacKenzie-Graham[1,*], **Seema K. Tiwari-Woodruff**[2,*], **Gaurav Sharma**[2], **Cynthia Aguilar**[1], **Kieumai T. Vo**[1], **Lauren V. Strickland**[1], **Laurie Morales**[2], **Boma Fubara**[3], **Melanie Martin**[4], **Russell E Jacobs**[5], **G. Allan Johnson**[3], **Arthur W. Toga**[1], and **Rhonda R. Voskuhl**[2]

[1]Laboratory of Neuro Imaging, Department of Neurology, University of California, Los Angeles.

[2]Multiple Sclerosis Program, Department of Neurology, University of California, Los Angeles.

[3]Center for In Vivo Microscopy, Duke University.

[4]Department of Physics, University of Winnipeg.

[5]Beckman Institute, California Institute of Technology.

Abstract

Gray matter atrophy observed by brain MRI is an important correlate to clinical disability and disease duration in multiple sclerosis. The objective of this study was to link brain atrophy visualized by neuroimaging to its underlying neuropathology using the MS model, experimental autoimmune encephalomyelitis (EAE). Volumetric changes in brains of EAE mice, as well as matched healthy normal controls, were quantified by collecting post-mortem high-resolution T2-weighted magnetic resonance microscopy and actively-stained magnetic resonance histology images. Anatomical delineations demonstrated a significant decrease in the volume of the whole cerebellum, cerebellar cortex, and molecular layer of the cerebellar cortex in EAE as compared to normal controls. The pro-apoptotic marker caspase-3 was detected in Purkinje cells and a significant decrease in Purkinje cell number was found in EAE. Cross modality and temporal correlations revealed a significant association between Purkinje cell loss on neuropathology and atrophy of the molecular layer of the cerebellar cortex by neuroimaging. These results demonstrate the power of using combined population atlasing and neuropathology approaches to discern novel insights underlying gray matter atrophy in animal models of neurodegenerative disease.

Keywords

cerebellum; gray matter atrophy; mouse; MRI; multiple sclerosis

Introduction

Gray matter atrophy is a common feature of many neurodegenerative diseases, including Alzheimer's disease (AD), Parkinson's disease (PD), and multiple sclerosis (MS). Atrophy

Corresponding author: Arthur W. Toga, Laboratory of Neuro Imaging, 635 Charles Young Drive South, Suite 225, Los Angeles, California 90095-1769, Telephone: (310) 206-2101, Fax: (310) 206-5518, toga@loni.ucla.edu.
*Both authors contributed equally and should both be considered first authors

has been linked to disability in all of these diseases (Camicioli et al., 2003; Chard et al., 2002; Firbank et al., 2007), underscoring its importance and the need to understand the mechanisms that drive it.

Multiple sclerosis has traditionally been viewed as an inflammatory, demyelinating disease of the central nervous system (CNS). Most patients begin with a relapsing-remitting form of the disease, characterized by inflammation and demyelination, which gradually transitions over several years to a secondary progressive form, characterized by progressive disability and tissue degeneration. A growing body of literature has documented the neurodegenerative aspect of MS (Evangelou et al., 2000; Peterson et al., 2001; Trapp et al., 1999). Whole brain atrophy was initially described in MS (Rudick et al., 1999) and several studies have since demonstrated a strong relationship between gray matter atrophy and disability (Ge et al., 2000; Rudick et al., 1999; Stevenson et al., 2000), including infratentorial and cerebellar atrophy (Edwards et al., 1999; Iannucci et al., 1999; Liu et al., 1999). Indeed, gray matter atrophy is now considered to be one of the most clinically relevant markers of MS disease progression (Fisher et al., 2002).

The primary function of the cerebellum is the modulation of movement; it plays a crucial role in coordination and balance. Clinical MS studies have found that fully one third of subjects have functionally relevant cerebellar deficits (Alusi et al., 2001; Weinshenker et al., 1996) and have demonstrated up to 19% decreases in cerebellar volume in MS patients (Edwards et al., 1999; Liu et al., 1999). Also, cerebellar atrophy in MS is closely correlated with disability on cerebellar functional subscales (Edwards et al., 1999; Liu et al., 1999). Thus, while cerebellar atrophy in MS has clinically relevant consequences, its underlying etiology remains poorly understood.

We have previously demonstrated gray matter atrophy in the cerebella of mice with experimental autoimmune encephalomyelitis (EAE), the most widely used model of MS, and found a correlation between this atrophy and disease duration (MacKenzie-Graham et al., 2006). Here, we have used neuroimaging to localize cerebellar atrophy within the cortical molecular layer and neuropathology to determine that Purkinje cell loss correlates with this atrophy. We examine the cellular etiology of the gray matter atrophy visualized by magnetic resonance imaging (MRI) and report that Purkinje cell loss is associated with it.

Materials and Methods

Mice

Female C57BL/6 mice, 8–12 weeks old, were purchased from the Jackson Laboratory. All studies were performed in accordance with approval from the UCLA Office of Protection of Research Subjects.

Antigen

Myelin oligodendrocyte glycoprotein (MOG) peptide 35–55 was purchased at greater than 98% purity (Chiron Mimotopes, Emeryville, CA).

EAE

Mice were immunized with MOG peptide 35–55 (300 µg/mouse) and Mycobacterium tuberculosis (500 µg/mouse) emulsified in Complete Freund's Adjuvant subcutaneously, in a volume of 0.1 ml/mouse over two sites: the right draining inguinal and axillary lymph nodes. One week later a booster immunization was delivered subcutaneously, over the contralateral draining lymph nodes. Pertussis toxin (500 ng/mouse) (List Biological Laboratories, Inc., Campbell, CA) was injected intraperitoneally on days 0 and 2 (Liu et al., 2003; Suen et al., 1997). EAE was graded on a scale of 0 to 5, based on difficulty with ambulation, as described

(Pettinelli and McFarlin, 1981). A total of five independent EAE groups were used in this study, extending from day 15 to day 147 after disease induction.

Magnetic Resonance Microscopy

Mice were perfused intracardially and post-fixed with 4% paraformaldehyde (Sigma-Aldrich, St. Louis, MO). After post-fixation the brains were incubated in PBS for 10–15 days prior to imaging. Magnetic resonance microscopy (MRM) was performed using an 89 mm vertical bore 11.7 T Bruker Avance imaging spectrometer with a micro-imaging gradient insert with a maximum gradient strength of 100 G/cm and 30 mm birdcage RF coil (Bruker Instruments, Billerica, MA). The brains were held in custom-made delrin holders in test tubes filled with Fomblin Perfluoropolyether (PFPE) YO4 grade (Ausimont USA, Inc., Thorofare, NJ) and maintained at 4°C. Typical imaging parameters were as follows: T2-weighted RARE 3D imaging protocol (8 echoes), matrix dimensions = $256 \times 256 \times 256$; FOV = 3 cm $\times$ 1.5 cm $\times$ 1.5 cm; repetition time (TR) = 1500 ms; effective time (TE) = 10 ms; number of averages = 4. The images were padded with zeros to double the number of time domain points in each dimension, the Fourier transformed to yield a matrix of $512 \times 256 \times 256$. This procedure is commonly called "zero-filling" and is a well known interpolation method (Farrar and Becker, 1971; Fukushima and Roeder, 1981). Typical spatial resolution was approximately 60 μm^3 per voxel.

Magnetic Resonance Histology

All magnetic resonance histology (MRH) (Johnson et al., 1993) was performed at the Duke Center for In Vivo Microscopy (CIVM), an NCRR/NCI National Resource. Specimens were actively stained for MR histology using a mixture of formalin and Prohance (Bracco, Princeton, NJ) to reduce the spin lattice relaxation time (T1) (Johnson et al., 2002a; Johnson et al., 2002b). Staining employed a multi-step transcardial perfusion in which pressure, temperature, and perfusate composition are carefully controlled to optimize the penetration of fixative and gadolinium contrast agent. Upon completion of the perfusion the head was removed and placed in a cylindrical acrylic container filled with perflourocarbon to limit susceptibility effects. The brain was scanned in the skull to limit physical distortion. This preparation permitted us to collect serial sections from the tissue after scanning.

All scanning was done at 9.4 T in a 12 mm diameter solenoid coil. Data were acquired with an RF refocused spin echo sequence. The sequence employs a sampling strategy in which Fourier space is sampled asymmetrically with $384 \times 384 \times 768$ points. The strategy samples one side of Fourier space (along all three axes) at the Nyquist frequency sufficient to support 21.5 micron spatial resolution. The unsampled points on the opposite side of Fourier space are zero filled. The dynamic range of the receiver is increased in the periphery of Fourier space to preferentially weight the higher frequencies resulting in a simultaneous reduction of scan time while maintaining the high spatial resolution. Data are displayed as magnitude images on a $512 \times 512 \times 1024$ array with effective isotropic spatial resolution of 21.5 microns. Scan time is 2.05 hrs.

Image Processing

MRM and MRH images were skull-stripped using the Brain Surface Extractor (BSE) within BrainSuite 2 (Shattuck and Leahy, 2001). Inaccuracies were corrected by manually editing the masks using BrainSuite 2. After skull-stripping, field inhomogeneities were corrected using N3 correction (Sled et al., 1998). A minimum deformation target (MDT) was produced as described (Kochunov et al., 2001). Each of the images was then linearly aligned to the MDT with a 12-parameter full-affine transformation using Alignlinear (AIR 5.2.5) (Woods et al., 1998a; Woods et al., 1998b) and the least squares with intensity rescaling cost function followed by a 5th-order polynomial warp using Align_warp (AIR). The images were then

resampled and averaged to produce the final minimum deformation atlas (MDA). The MDA was then aligned to a standard atlas (MacKenzie-Graham et al., 2004) to permit the direct comparison of images in a standard space. All automated image processing was performed in the LONI Pipeline Processing Environment (Rex et al., 2003) using either a 32-processor Onyx 200 or 64-processor Origin 3000 supercomputer (SGI).

Anatomical Delineations

A blinded expert neuroanatomist using BrainSuite 2 manually delineated anatomical structures on the MDA. Cerebellar delineations included cerebellar cortex, the molecular layer of the cerebellar cortex, and cerebellar white matter. Cerebellar cortex delineations rigorously excluded white matter and partial volume voxels. Molecular layer of the cerebellar cortex delineations were made taking advantage of the contrast between the molecular layer of the cerebellar cortex and the granule cell layer provided by the active stained MRH scans. Anatomical delineations were based on the Mouse Atlas Project 2003 mouse brain atlas (MacKenzie-Graham et al., 2004).

Image Analysis

Images were spatially normalized with a 12-parameter full-affine transformation to register each image to the MDA using Alignlinear (AIR). In order to intensity normalize the images the alignment was performed with an intensity rescaling cost function. Align_warp (AIR) was used to compute 5th-order polynomial mappings of the MDA to each individual normalized brain. These mappings were then used to warp the anatomical delineations from the MDA to each of the individual images. Individual delineations were then manually corrected in BrainSuite 2.

Immunohistochemistry

After magnetic resonance histology (MRH), brains were removed from the skull and prepared for sectioning. 50 μm sagittal frozen sections were cut using a CM3050S cryostat (Leica Microsystems, Wetzlar, Germany). Free-floating sections were permeabilized in 0.3% Triton X-100 in PBS and blocked with 10% normal goat serum (Vector Laboratories, Burlingame, CA). White matter immunostaining was enhanced by treating sections with 95% ethanol/5% acetic acid for 15 minutes prior to permeabilization and blocking. Specific cell types and structures, sections were pre-incubated with primary antibodies in PBS solution containing 2% NGS for 2 hours at room temperature, then overnight at 4°C. The following primary antibodies were used: rabbit anti-parvalbumin (1:1000) (Millipore, Billerica, MA), rat anti-myelin basic protein (1:500) (Millipore), rat anti-CD45 (1:1000) (Millipore), mouse anti-NeuN (1:500) (Millipore), rabbit or mouse anti-caspase-3 (1:250) (Millipore), rabbit anti-synapsin (1:500) (Millipore), rabbit anti-neurofilament-NF200 (1:1000) (Sigma-Aldrich), mouse or rabbit anti-calbindin-2 (1:750)(Sigma-Aldrich). Fluorescence secondary antibody labeling included antibodies conjugated to TRITC, FITC, and Cy5 (Vector Laboratories and Millipore). Chromogen immunohistochemistry was performed, after avidin-biotin block, by incubating with mouse anti-caspase-3 (Millipore) alone or sequentially with rabbit anti-calbindin-2 (Sigma-Aldrich) followed by biotinylated secondary antibody. A streptavidin-peroxidase conjugate was added, followed by the addition of the chromogen (blue/gray or red; Vector Laboratories). The sections were mounted, dehydrated and coverslipped with Permount (Fisher Scientific, Pittsburgh, PA). IgG-control experiments were performed for all primary antibodies, and no staining was observed under these conditions. To assess the number of cells, 4',6'-diamidino-2-phenylindole dihydrochloride (DAPI 2ng/ml; Invitrogen, Carlsbad, CA) was added for 15 minutes prior to final washes after secondary antibody addition. The sections were mounted on slides, dried, and coverslipped with fluoromount G (Fisher Scientific). Both mouse

and rabbit anti-caspase-3 and anti-calbindin-2 antibodies were used to permit different staining combinations. Staining was comparable between mono- and polyclonal antibodies.

Microscopy and Analysis

Confocal images of immunostained sections were photographed using a spin-disc (Olympus, Center Valley, PA) and TCS-SP laser confocal microscope (Leica Microsystems) with a digital camera (Hamamatsu Photonics, Bridgewater, NJ). All images were collected using similar acquisition parameters. Photomicrographs of each representative experimental group were collected and analyzed with ImageJ software (v1.36b).

The degree of demyelination and inflammation in cerebellar white and gray matter was assessed by quantifying anti-MBP and anti-CD45 staining by optical density. Confocal stacks of immunolabeled images from each animal were processed with a series of manual and automated procedures that included the following steps: (1) the images were oriented in the same direction, (2) the RGB channels of the images were split and converted to 8 bit gray images in Image J, (3) gray matter (granule cell, Purkinje cell and molecular layer) and white matter was manually delineated on the basis of DAPI staining, and (4) threshold gray matter and white matter density was calculated and reported as a percentage of total area.

Synapsin staining density in the molecular layer of the cerebellar cortex was assessed by quantifying anti-synapsin staining by optical density. Confocal stacks of immunolabeled images from each animal were processed with a series of manual and automated procedures that included the following steps: (1) the images were oriented in the same direction, (2) the RGB channels of the images were split and converted to 8 bit gray images in Image J, (3) the molecular layer was manually delineated on the basis of DAPI staining, and (4) threshold synapsin staining density was calculated and reported as a percentage of total area.

Cell Counts

Purkinje cells were quantified by counting calbindin-2$^+$ cell bodies in the Purkinje layer of 4X and 10X images of the entire cerebellum. Fluorescence-stained sections were counted using z-stacks with at least 15–20 optical sections 2 µm apart. Every third optical section was analyzed and averaged. Dehydration in chromogen-stained sections does not permit many z-planes to be available, so here we counted Purkinje cells in a projected image. Results from the chromogen-stained sections were similar to fluorescent sections. Three to five brain sections (50 µm thick) 200 µm apart were analyzed from each animal (control: n = 5; EAE: n = 7). All sections counted were close to midline. In every analysis, the same areas from EAE and normal mice were assessed. Only cells with their entire nucleus present in the section were counted. Some animals were excluded from the analysis due to incomplete perfusion or because the tissue was damaged. Blinded cell counting was performed using lobules I/II and III to estimate and compare the total number of Purkinje cells. These lobules were chosen since lobules I/II and III were consistently present in all tissue sections, whereas other lobules were missing from some preparations and thus could not be used for comparisons among all the mice. Additional cell counts were performed on a subset of tissue sections where the entire cerebellum was present. While the total number of sections where the entire cerebellum was intact was reduced, these counts showed a similar pattern when comparing EAE mice and controls as that observed when lobules I/II and III were examined (data not shown). Furthermore, another set of sections was examined in which lobules IV, IX and X were intact and again the same pattern was observed as in lobules I/II and III (data not shown).

Statistics

All results are presented as mean ± SEM, and statistical differences were determined by the Welch's t-test. Regression analysis and Welch's t-tests were performed in Excel (Microsoft).

Comparisons across EAE time points were subject to *post hoc* multiple comparisons confounds, so the results of the Bonferroni correction ($p < \alpha/n$) were considered.

Results

MOG-induced EAE in C57BL/6 has a chronic progressive disease course. The literature focuses primarily on disease in the spinal cord, but inflammation and focal lesions have been demonstrated in the cerebellum and forebrain as well (Black et al., 2006; Carter et al., 2007; Kuerten et al., 2007; Lees et al., 2008; MacKenzie-Graham et al., 2006; Melzer et al., 2008; Selvaraj and Geiger, 2008; Uemura et al., 2008). Mice with this form of EAE develop focal lesions that are easily identifiable by T2-hyperintensities in the cerebellar white matter, brain stem, and spinal cords. These lesions are readily detected at day 15 after disease induction (Fig. 1A). We were able to confirm that the T2-hyperintensities in the MRM images were white matter lesions by histology, using a reducing silver myelin stain combined with Nissl-staining for cell bodies. Indeed, our C57BL/6J mice with MOG 35–55 induced active EAE demonstrated significant focal lesions in the cerebellar white matter (Figs. 1B & C), brainstem, and spinal cord (day 55). Here we will focus on the remote effects of white matter lesions on gray matter using neuroimaging and neuropathology.

An MRM Atlas of EAE Brain

In order to address the issue of gray matter atrophy in mice with EAE, we acquired post-mortem T2-weighted magnetic resonance microscopy (MRM) scans from two independent EAE groups totaling 32 mice. The active induction model of EAE in the C57BL/6 mouse with myelin oligodendrocyte glycoprotein (MOG) was used. This model is characterized by disease onset at 12–14 days post-induction followed by chronic disability. 5 mice were sacrificed early in disease (day 15), 8 mice in the middle stages of disease (day 35–47), 8 mice late in disease (day 48–57) and scanned. 11 strain-, age-, and sex-matched healthy controls were also sacrificed and scanned. All the scans were skull-stripped semi-automatically and corrected for field inhomogeneity.

A minimum deformation atlas (MDA) was constructed from the 32 MRM scans collected. The MDA was then aligned to a standard atlas (MacKenzie-Graham et al., 2004) to permit the direct volumetric comparison of images in a standard space. The standard minimum deformation atlas then served as a target space for the spatial and intensity normalization of the original images, correcting both gross size differences and gross intensity differences. Following creation of this atlas, anatomical structures (e.g. whole cerebellum, cerebellar cortex, cerebellar white matter) were manually delineated on that atlas (Fig. 2). The delineations were then warped onto the images that were used to create the atlas to produce standardized estimates of regional atrophy in individual subjects.

Atrophy in the Cerebella of Mice with Late EAE

Mice with EAE demonstrate motor deficits that may reflect damage to corticospinal and/or spinocerebellar tracts. MOG-induced EAE is known to induce spinal cord and cerebellar white matter lesions, so we hypothesized that atrophy of the cerebellum might occur as a remote effect of transection of spinocerebellar or other cerebellar white matter tracts. We found a significant reduction in cerebellar volume in mice with late EAE compared to normal controls. The volume of the cerebellum in normal mice had mean of 48.2 ± 0.3 mm^3. Mice in the late stages of EAE had a mean cerebellar volume of 45.0 ± 0.7 mm^3. This reflected a 6.6% decrease in cerebellar volume ($p = 0.0036$).

Brain atrophy has been shown to correlate with disease duration in MS (Ge et al., 2000; Kalkers et al., 2001), so we examined the relationship between cerebellar volume and disease duration

in mice with EAE. We performed a regression analysis to determine if disease duration correlated with cerebellar volume in mice with EAE. There was an inverse correlation between cerebellar volume and disease duration, indicating that atrophy occurs progressively during disease as a function of time (Figs. 3A & B) (R = −0.6178, n = 21, p = 0.0028). The disease course for this cohort of mice is overlaid on the graph for illustrative purposes (Fig. 3B).

No Significant Atrophy in the Cerebellar White Matter of Mice with EAE

Lesions are known to occur in cerebellar white matter tracts in EAE and it was possible that some of the atrophy detected in whole cerebellum was occurring in the white matter tracts. We measured the volumes of the cerebellar white matter in mice with MOG-induced EAE and normal controls. The volume of the cerebellar white matter in normal mice had mean of 6.60 ± 0.14 mm^3. Mice in the late stages of EAE had a mean cerebellar white matter volume of 6.28 ± 0.22 mm^3. This decrease in cerebellar white matter volume did not reach statistical significance (p = 0.12). We performed a regression analysis to determine if disease duration correlated with cerebellar white matter volume in mice with EAE. There was no correlation between disease duration and cerebellar white matter volume (Figs. 3C & D) (R = −0.0747, n = 21, p = 0.75). The disease course for this cohort of mice is overlaid on the graph for illustrative purposes (Fig. 3D).

Atrophy in the Cerebellar Cortex of Mice with late EAE

In order to assess whether the atrophy discovered in whole cerebellum was occurring primarily in the gray matter, we measured the volumes of the cerebellar cortex in mice with EAE and normal controls. We found a significant reduction in cerebellar cortex volume in mice with late EAE compared to normal controls. The volume of the cerebellar cortex in normal mice had mean of 39.7 ± 0.3 mm^3. Mice in the late stages of EAE had a mean cerebellar cortex volume of 36.9 ± 0.8 mm^3. This reflected a 7.2% decrease in cerebellar cortex volume (p = 0.0047). We performed a regression analysis to determine if disease duration correlated with cerebellar cortex volume in mice with EAE. There was an inverse correlation between cerebellar cortex volume and disease duration, indicating that cerebellar cortex atrophy occurs progressively during disease as a function of time (Figs. 3E & F) (R = −0.6207, n = 21, p = 0.0027). The disease course for this cohort of mice is overlaid on the graph for illustrative purposes (Fig. 3F).

An MRH Atlas of EAE Brain

In order to further localize the gray matter atrophy in the cerebellum, we acquired post-mortem MRH scans from two additional independent EAE groups totaling 21 mice. Differences in the contrast between the MRH and MRM scans allowed us to unambiguously delineate the molecular layer of the cerebellar cortex (Fig. 2 B & C). We had appreciated from the initial experiments that atrophy was progressing as a function of time, thus we chose later time points to increase our chances of being able to localize the precise gray matter layer in the cerebellum that was undergoing atrophy. 10 mice very late in disease (day 61–147) and 11 strain, age, and sex matched healthy controls were also sacrificed and imaged. All the scans were skull-stripped semi-automatically and corrected for field inhomogeneity.

A minimum deformation atlas was constructed from the 21 MRH scans collected. The MDA was then aligned to a standard atlas (MacKenzie-Graham et al., 2004) to permit the direct volumetric comparison of images in a standard space. The standard minimum deformation atlas then served as a target space for the spatial and intensity normalization of the original images, correcting both gross size and intensity differences. Following creation of this atlas, anatomical structures were manually delineated on that atlas and then warped onto the images that were used to create the atlas to produce standardized estimates of regional gray matter loss in individual subjects. Though the MRH scans were acquired on a different scanner using a

different protocol than the MRM scans, alignment of the images to a standard space allowed direct volumetric comparison of MRM and MRH images. We used the MRH images to further localize the region in which gray matter atrophy was occurring.

Atrophy in the Molecular Layer of the Cerebellar Cortex of Mice with EAE

In this second independent experiment, we again found atrophy in the whole cerebellum and in addition found atrophy in the molecular layer of the cerebellar cortex in mice with late EAE compared to normal controls. The volume of the whole cerebellum in normal mice had a mean of 48.3 ± 0.3 mm^3. Mice in the late stages of EAE had a mean whole cerebellar volume of 46.1 ± 0.4 mm^3. This reflected a 4.6% decrease in cerebellar volume (p = 0.05). The volume of the molecular layer of the cerebellar cortex in normal mice had mean of 30.5 ± 0.6 mm^3. Mice in the late stages of EAE had a mean molecular layer of the cerebellar cortex volume of 28.2 ± 0.6 mm^3. This reflected a 7.3% decrease in molecular layer of the cerebellar cortex volume (p = 0.0086). We performed a regression analysis to determine if disease duration correlated with volume of the molecular layer of the cerebellar cortex in mice with EAE. There was an inverse correlation between the volume of the molecular layer of the cerebellum and disease duration, indicating that cerebellar cortical atrophy in the molecular layer occurs progressively during disease as a function of time (Figs. 3G & H) (R = −0.6562, n = 10, p = 0.039). The disease course for this cohort of mice is overlaid on the graph for illustrative purposes (Fig. 3H).

No Atrophy in a Control Region in Mice with EAE

To determine whether the atrophy observed in cerebellar gray matter during late EAE represented some generalized phenomenon related to chronic disease (dehydration, etc.), as opposed to reflecting regionally specific gray matter atrophy, we measured the volumes of an area unlikely to be greatly affected by EAE, the olfactory area, as a negative control. Measurements of the volumes of the olfactory area from both MRM and MRH imaged mice were then subjected to the same statistical and regression analysis. There was no significant difference in olfactory area volume between mice with EAE and normal controls and the correlation observed during analysis of cerebellar cortex was not observed in this control region (data not shown). These data indicate that cerebellar gray matter atrophy in the molecular layer during late EAE was regionally specific.

Demyelination in the Cerebella of Mice with EAE

Once we had established that the largest part of the gray matter atrophy that we observed was in the molecular layer of the cerebellar cortex, we looked for pathological correlates in tissue collected from the mice that had been MRH imaged. As expected, we observed demyelination in the cerebellar white matter of mice with EAE (Fig. 4D). At higher magnification, we were able to identify lesions that were not only demyelinated, but were devoid of axons (Fig. 4E). Furthermore, we observed areas of demyelination in the granule cell layer of the cerebellar cortex and the presence of swollen axons and/or axon retraction bulbs (Fig. 4F) similar to those described previously in the brains of MS patients (Trapp et al., 1998). Demyelination was absent from normal age, sex, and strain matched controls (Figs. 4A–C). Upon quantification, we found a significant difference in the myelin basic protein (MBP) staining density in the cerebella of mice with EAE compared to normal controls (p < 0.00005).

Regression analysis demonstrated that MBP staining density in the cerebellar white matter had a direct correlation with the volume of the molecular layer of the cerebellar cortex (R = 0.6132, n = 12, p = 0.03398) (Fig. 4G). Similarly, a regression analysis demonstrated that MBP staining density in the cerebellar cortex had a direct correlation with the volume of the molecular layer of the cerebellar cortex (R = 0.8069, n = 12, p = 0.001514) (Fig. 4H). These data indicate that demyelination is associated with gray matter atrophy in the cerebella of mice with MOG-induced EAE.

Inflammation in the Cerebella of Mice with EAE

As expected, we observed extensive inflammatory cellular staining in the cerebella of mice with EAE (Fig. 5D). At higher magnification, we were able to identify CD45+ cells with a rounded morphology in the cerebellar white matter (Fig. 5E) and CD45+ cells with an activated microglia-like morphology in the molecular layer of the cerebellar cortex (Fig. 5F). CD45 immunostaining in normal age, sex, and strain-matched controls identified only occasional ramified microglia (Fig. 5A–C). Upon quantification, we found a significant difference in CD45+ staining density in the cerebella of mice with EAE compared to normal controls ($p < 0.00005$).

Regression analysis demonstrated that the number of CD45+ cells in the cerebellar white matter had an inverse correlation with the volume of the molecular layer of the cerebellar cortex ($R = -0.6942$, $n = 12$, $p = 0.01226$) (Fig. 5G). Similarly, a regression analysis demonstrated that CD45+ staining density in the cerebellar cortex had an inverse correlation with the volume of the molecular layer of the cerebellar cortex, but this trend did not reach statistical significance ($R = -0.5345$, $n = 12$, $p = 0.07338$) (Fig. 5H). These data indicate that white matter CD45+ staining density is associated with gray matter atrophy in the cerebella of mice with MOG-induced EAE.

Characterization of CD45+ cells in the Cerebella of Mice with EAE

Although CD45 is a marker for inflammatory cells, it does not discriminate the lineage of the cells it labels. In order to better characterize the CD45+ cells we observed in mice with EAE, we stained with CD3 (T-cells) and Mac-3 (macrophages and activated microglia). The CD45+ cells in the cerebella of mice with EAE comprised both CD3+ and Mac-3+ cells. Interestingly, both CD3+ and Mac-3+ cells were present in both the cerebellar white matter (Figs. 6A & C) and in all layers of the cerebellar cortex (Figs. 6B & D). White matter images (Figs. 6A & C) were centered on blood vessels to demonstrate continuing cellular infiltration even late in disease. Gray matter images (Figs. 6B & D) were focused on areas of intense cellular infiltration to visualize cellular morphology.

Apoptosis in the Cerebellar Cortex of Mice with EAE

Gray matter inflammation, demyelination, and atrophy led us to investigate if neurons in the cerebellar cortex were undergoing apoptotic cell death. We selected one of the most downstream effector molecules in the apoptosis pathway, caspase-3. Using antibodies for activated caspase-3, we observed an almost complete absence of staining from healthy controls (Figs. 7A–C). However, we observed substantial immunostaining in the cerebella of mice with EAE, not only in the cerebellar white matter, but also in the granule cell layer of the cerebellar cortex, and particularly in the Purkinje layer of the cerebellar cortex (Fig. 7D). At higher magnification, we were able to identify caspase-3+ cells with a Purkinje cell-like morphology (Fig. 7E) in mice with EAE. Double staining with caspase-3 and calbindin-2 verified that these cells were in fact Purkinje cells (Fig. 7F). Upon quantification, we found a significant difference in the number of caspase-3+ Purkinje cells in the cerebella of mice with EAE compared to normal controls ($p < 0.00005$). The number of the caspase-3+ Purkinje cells in normal mice had a mean of 0.65 ± 0.033 per lobule. Mice in the late stages of EAE had a mean of 7.2 ± 1.43 per lobule. This reflected a 10-fold increase in the number of caspase-3+ Purkinje cells in EAE. Purkinje cells also expressed terminal deoxynucleotidyl transferase dUTP nick end labeling (TUNEL) staining in mice with EAE (data not shown).

Decreased Purkinje Cell Number in the Cerebella of Mice with EAE

We further investigated Purkinje cell pathology in the cerebella of mice with EAE. Calbindin-2 immunostaining demonstrated a disruption of the normal anatomy of the Purkinje and

molecular layers of the cerebellar cortex compared to normal controls (Figs. 8A & C). At higher magnification we observed an overall disorganization, changes in dendritic arborization, a reduction in cell soma size, and a decrease in the numbers of Purkinje cells in mice with EAE compared to normal control mice (Figs. 8B & D). Upon quantification, we found a significant decrease in the number of calbindin-2$^+$ cells in the cerebella of mice with EAE as compared to normal controls. Specifically, the number of the calbindin-2$^+$ cells in normal mice had a mean of 113.5 ± 5.5, while mice in the late stages of EAE had a mean of 86.0 ± 6.0. This reflected a 24.2% decrease in the number of calbindin-2$^+$ cells ($p < 0.001$).

Regression analysis demonstrated that the number of calbindin-2$^+$ cells had a direct correlation with the volume of the molecular layer of the cerebellar cortex ($R = 0.6287$, $n = 11$, $p = 0.03826$) (Fig. 8E). These data indicate that Purkinje cell loss is associated with gray matter atrophy in the cerebella of mice with MOG-induced EAE.

It is possible that the decrease we observed in dendritic arborization could due to the redistribution of calbindin-2 from intact dendrites to the cell body (Wang et al., 2007). In order to address this we selected synapsin to evaluate the synaptic density of neurons in the cerebellar cortex. Synapsin staining was decreased in mice with EAE compared to normal controls (Fig. 9). The synapsin staining density in the molecular layer of the cerebellar cortex in normal mice had mean of $55.7 \pm 1.7\%$. Mice in the late stages of EAE had a mean synapsin staining density in the molecular layer of the cerebellar cortex of $15.2 \pm 7.1\%$. This reflected a 73% decrease in synapsin staining density in the molecular layer of the cerebellar cortex ($p = 0.016$). These data are consistent with dendritic arborization loss in Purkinje cells in mice with EAE.

Time Course of Inflammatory Changes in the Cerebella of Mice with EAE

Cross modality correlation of MRI with pathology revealed several associations with atrophy: inflammation, demyelination, and Purkinje cell loss. In order to further discern the sequence of neuropathological events, we used a complementary approach. We had previously found significant cerebellar cortical atrophy at day 55 of EAE, but not at day 15 or day 35 (MacKenzie-Graham et al., 2006). Therefore an additional set of 17 mice was studied to determine the sequence of neuropathological events preceding the onset atrophy at day 55. Mice were sacrificed at three time points during disease, days 15, 35, and 55. Strain, age, and sex matched healthy controls were also sacrificed in parallel at each time point. We observed extensive inflammatory cell staining in the cerebella of mice with EAE. Significant CD45 immunoreactivity was observed in the white matter of cerebellar sections beginning in EAE mice at day 15. Upon quantification, CD45 staining in white matter peaked at day 35, and then at day 55 returned to levels that were not significantly different from levels at day 15 in EAE (Fig. 10A). At all time points EAE mice had significantly more CD45 white matter staining than controls ($p > 0.05$).

In general, CD45 staining in gray matter was much less than in white matter. Importantly, in contrast with white matter staining, CD45 immunoreactivity in the gray matter appeared to increase continuously with time in EAE (Fig. 10B). Specifically, later disease time points had greater CD45 staining than earlier time points. At all time points mice with EAE had significantly more CD45 gray matter staining than controls ($p > 0.05$). Notably, a substantial increase in white matter CD45$^+$ staining at day 35 preceded previously documented gray matter atrophy (MacKenzie-Graham et al., 2006) at day 55, while gray matter CD45$^+$ staining was highest at a time that coincided (day 55) with gray matter atrophy.

Time Course of Demyelination in the Cerebella of Mice with EAE

MBP immunoreactivity was measured to explore the state of myelination in both white and gray matter at each time point in this set of mice dedicated to examining the time course of

neuropathological events that precede atrophy detection by MRI. Throughout the time course, control tissue showed dense MBP staining in the central white matter tracts, with regular, parallel arrays of myelinated axons radiating into the granule cell layer. As expected, white matter myelination was substantially greater than gray matter myelination. Quantification indicated that white matter MBP immunoreactivity was significantly lower in EAE mice than controls at all time points ($p > 0.05$) (Fig. 10C). Cross comparison within EAE showed that subsequent time points had lower MBP immunoreactivity values than at day 15. Decreases in gray matter MBP immunoreactivity occurred primarily in regions juxtaposed to white matter lesions. However, some lesions extended directly from white matter into the granule cell layer. Gray matter MBP immunoreactivity in EAE showed a decreasing trend that reached significance ($p > 0.05$) at day 55 (Fig. 10D). Notably, white matter demyelination at day 35 preceded gray matter atrophy previously documented at day 55 (MacKenzie-Graham et al., 2006), while gray matter demyelination reached significance coincident with gray matter atrophy at day 55.

Time Course of Purkinje Cell Number in the Cerebella of Mice with EAE

We assessed Purkinje cell number at each time point to determine when Purkinje cell loss occurred relative to the above sequence of inflammatory and demyelinating events. Differences in Purkinje cell density between control and EAE mice were not observed early in disease, at days 15 and 35 (Fig. 10E). However, EAE mice had substantially decreased neuronal density in the Purkinje layer at day 55 as compared to age matched controls. This appeared to be due to the loss of calbindin-2$^+$ Purkinje cells. By day 55 substantial numbers of Purkinje cells were absent (Fig. 8). Age matched controls did not display these characteristics at any time point. The decrease in Purkinje cell number showed a precise temporal correlation with previously documented gray matter atrophy measured by MRI at day 55 in EAE (MacKenzie-Graham et al., 2006).

Discussion

MS is an inflammatory, demyelinating disease of the central nervous system (CNS) that results in damage to myelin, oligodendrocytes, axons, and neurons. Inflammation, demyelination, and neurodegeneration are intimately tied together (Geurts and Barkhof, 2008), and although MRI cannot establish the mechanisms of neurodegeneration, increasingly sophisticated imaging and analysis techniques are making it possible to determine precisely where and when it occurs. Here we have determined that, in the most widely used model for MS, the loss of Purkinje cells is clearly associated with gray matter atrophy in the molecular layer of the cerebellum. This is especially relevant in light of findings in MS which demonstrated not only demyelination, but Purkinje cell loss in the cerebellar cortex (Kutzelnigg et al., 2007).

There is a growing body of evidence that the cerebellum is targeted in several models of EAE. Though MOG peptide induced EAE is one of the most commonly used models of EAE, many models are used, each with subtly different disease courses and pathologies. Disruption of the blood-brain barrier (BBB) at the cerebellum occurs early in disease in Lewis rats as visualized using ultra small particles of iron oxide (USPIO) in MRI (Floris et al., 2004; Rausch et al., 2003). The same has been shown in SJL/J mice with proteolipid protein (PLP) peptide 139–151-induced EAE, where cerebellar BBB breakdown was demonstrated to occur prior to disruption of the BBB in the spinal cord and prior to the development of clinical symptoms (Tonra, 2002; Tonra et al., 2001). Interestingly, this work demonstrated that the rabbit immunoglobulins used to evaluate BBB breakdown accumulated around Purkinje cells. In an atypical model of EAE in C3H/HeJ mice immunized with PLP peptide 190–209 BBB disruption and cellular infiltration were also shown in the cerebellum (Muller et al., 2005). These findings are all consistent with our observations of inflammatory cell infiltration in the

cerebellum as early as day 15. Furthermore, tumor necrosis factor (TNF)-related apoptosis-inducing ligand (TRAIL) has also been reported to induce caspase-3 mediated cell death in the brainstems of SJL/J mice immunized with PLP peptide 139–151 (Aktas et al., 2005), reinforcing our finding that neuronal cell death is occurring during EAE.

In MS, if an axon is not transected by inflammatory segmental demyelination, redistribution of sodium channels can re-establish conduction across the demyelinated segment and improve function (Craner et al., 2004). However, this increases the energy demands of neuronal conduction and renders the demyelinated axon more susceptible to hypoxic/ischemic damage (Dutta et al., 2006). Furthermore, these channels do not have the same electrical characteristics as the original ones and may be responsible for some MS symptoms. Purkinje cells are the only output neurons of the cerebellar cortex and are critical in motor coordination, learning, and timing (Mauk et al., 2000). There is a growing body of evidence suggesting that abnormal expression of sodium channels may distort the pattern of Purkinje cell firing and thus contribute to cerebellar ataxia in MS and EAE (Black et al., 2000; Craner et al., 2003; Craner et al., 2004; Damarjian et al., 2004; Waxman, 2005). Specifically, expression of Nav1.8 (SNS) is upregulated in expression in Purkinje cells in mice with EAE and humans with MS. This aberrant expression was associated with altered Purkinje firing patterns, with high-frequency sustained firing in response to prolonged depolarization, a factor that could lead to energy deprivation in these neurons (Renganathan et al., 2003). Our finding of Purkinje cell loss in this study is consistent with the hypothesis that abnormal channel expression can render a neuron susceptible to cell death in EAE. In addition, we observed a disorganization and decrease in the dendritic arborization of Purkinje cells in mice with EAE. Furthermore, our observation of decreased synapsin staining density in the molecular layer of the cerebellar cortex is consistent with a decrease in Purkinje cell dendritic arborization and with the literature describing decreases in synapsin expression in the spinal cords of mice with EAE (Nicot et al., 2005) and decreases in dendritic spine density and arbors, along with atrophy of the cell body and/or complete cell loss (Bannerman et al., 2005).

Cerebellar atrophy in MS is closely correlated with disability on cerebellar functional subscales (Edwards et al., 1999; Liu et al., 1999), however it has often been attributed to tract degeneration. In the murine cerebellum, white matter tracts contribute only 14% of the volume, and though there was a trend toward some white matter atrophy in mice with EAE, this change in cerebellar white matter volume did not account for the majority of the reduction in cerebellar volume in mice with EAE. Cerebellar cortex volume loss, not white matter volume loss, accounted for the majority of the cerebellar atrophy we observed. However, we cannot rule out gray matter atrophy in other cerebellar structures, such as the deep cerebellar nuclei or the granule cell layer of the cerebellar cortex.

At very late time points (day 61–147), we found that cortical atrophy correlated with white matter inflammation (Fig. 5). Further data collected, from a different cohort of EAE mice, indicated that the level of white matter inflammation at the late time points was less than the level of white matter inflammation at day 35 (Fig. 10). Notably, higher levels of white matter inflammation relatively early in disease (day 35) do not preclude the possibility that low levels of chronic white matter inflammation late in disease could correlate with gray matter atrophy. Interestingly, our data show that high levels of inflammation in white matter at day 35 do not correlate with concurrent gray matter atrophy at this earlier time point, since very little gray matter atrophy was observed at day 35 (MacKenzie-Graham et al., 2006). This could be due to a variety of reasons. For example, white matter inflammation may require time to induce neurodegenerative changes in remote gray matter regions. Indeed, in contrast to late time points, we have not seen caspase-3[+] or TUNEL^{+} Purkinje cells in the cerebella of mice with EAE at relatively early time points (day 15–47; unpublished observations). This is consistent with Purkinje cell death occurring only when cerebellar atrophy is measurable.

In summary, we have demonstrated for the first time that atrophy of a gray matter structure which occurs during autoimmune mediated demyelination is associated with histopathological evidence of widespread caspase-3 mediated cell death of a major neuronal cell type within this structure. Understanding relationships such as these will permit the future design of rational neuroprotective strategies to prevent gray matter atrophy and disability accumulation during EAE, and possibly MS. Finally, cross-modality correlations between imaging and pathologic data, as described herein, may be a useful approach in a variety of neurodegenerative disease models.

Acknowledgements

References

Aktas O, Smorodchenko A, Brocke S, Infante-Duarte C, Schulze Topphoff U, Vogt J, Prozorovski T, Meier S, Osmanova V, Pohl E, Bechmann I, Nitsch R, Zipp F. Neuronal damage in autoimmune neuroinflammation mediated by the death ligand TRAIL. Neuron 2005;46:421–432. [PubMed: 15882642]

Alusi SH, Worthington J, Glickman S, Bain PG. A study of tremor in multiple sclerosis. Brain 2001;124:720–730. [PubMed: 11287372]

Bannerman PG, Hahn A, Ramirez S, Morley M, Bonnemann C, Yu S, Zhang GX, Rostami A, Pleasure D. Motor neuron pathology in experimental autoimmune encephalomyelitis: studies in THY1-YFP transgenic mice. Brain 2005;128:1877–1886. [PubMed: 15901645]

Black JA, Dib-Hajj S, Baker D, Newcombe J, Cuzner ML, Waxman SG. Sensory neuron-specific sodium channel SNS is abnormally expressed in the brains of mice with experimental allergic encephalomyelitis and humans with multiple sclerosis. Proceedings of the National Academy of Sciences of the United States of America 2000;97:11598–11602. [PubMed: 11027357]

Black JA, Liu S, Hains BC, Saab CY, Waxman SG. Long-term protection of central axons with phenytoin in monophasic and chronic-relapsing EAE. Brain 2006;129:3196–3208. [PubMed: 16931536]

Camicioli R, Moore MM, Kinney A, Corbridge E, Glassberg K, Kaye JA. Parkinson's disease is associated with hippocampal atrophy. Mov Disord 2003;18:784–790. [PubMed: 12815657]

Carter SL, Muller M, Manders PM, Campbell IL. Induction of the genes for Cxcl9 and Cxcl10 is dependent on IFN-gamma but shows differential cellular expression in experimental autoimmune encephalomyelitis and by astrocytes and microglia in vitro. Glia 2007;55:1728–1739. [PubMed: 17902170]

Chard DT, Griffin CM, Parker GJ, Kapoor R, Thompson AJ, Miller DH. Brain atrophy in clinically early relapsing-remitting multiple sclerosis. Brain 2002;125:327–337. [PubMed: 11844733]

Craner MJ, Kataoka Y, Lo AC, Black JA, Baker D, Waxman SG. Temporal course of upregulation of Na(v)1.8 in Purkinje neurons parallels the progression of clinical deficit in experimental allergic encephalomyelitis. J Neuropathol Exp Neurol 2003;62:968–975. [PubMed: 14533785]

Craner MJ, Newcombe J, Black JA, Hartle C, Cuzner ML, Waxman SG. Molecular changes in neurons in multiple sclerosis: altered axonal expression of Nav1.2 and Nav1.6 sodium channels and Na+/Ca2+ exchanger. Proceedings of the National Academy of Sciences of the United States of America 2004;101:8168–8173. [PubMed: 15148385]

Damarjian TG, Craner MJ, Black JA, Waxman SG. Upregulation and colocalization of p75 and Nav1.8 in Purkinje neurons in experimental autoimmune encephalomyelitis. Neuroscience Letters 2004;369:186–190. [PubMed: 15464262]

Dutta R, McDonough J, Yin X, Peterson J, Chang A, Torres T, Gudz T, Macklin WB, Lewis DA, Fox RJ, Rudick R, Mirnics K, Trapp BD. Mitochondrial dysfunction as a cause of axonal degeneration in multiple sclerosis patients. Ann Neurol 2006;59:478–489. [PubMed: 16392116]

Edwards SG, Gong QY, Liu C, Zvartau ME, Jaspan T, Roberts N, Blumhardt LD. Infratentorial atrophy on magnetic resonance imaging and disability in multiple sclerosis. Brain 1999;122(Pt 2):291–301. [PubMed: 10071057]

Evangelou N, Esiri MM, Smith S, Palace J, Matthews PM. Quantitative pathological evidence for axonal loss in normal appearing white matter in multiple sclerosis. Ann Neurol 2000;47:391–395. [PubMed: 10716264]

Farrar, TC.; Becker, ED. Pulse and Fourier Transform NMR. New York: Academic Press; 1971.

Firbank MJ, Blamire AM, Krishnan MS, Teodorczuk A, English P, Gholkar A, Harrison R, O'Brien JT. Atrophy is associated with posterior cingulate white matter disruption in dementia with Lewy bodies and Alzheimer's disease. Neuroimage 2007;36:1–7. [PubMed: 17412610]

Fisher E, Rudick RA, Simon JH, Cutter G, Baier M, Lee JC, Miller D, Weinstock-Guttman B, Mass MK, Dougherty DS, Simonian NA. Eight-year follow-up study of brain atrophy in patients with MS. Neurology 2002;59:1412–1420. [PubMed: 12427893]

Floris S, Blezer EL, Schreibelt G, Dopp E, van der Pol SM, Schadee-Eestermans IL, Nicolay K, Dijkstra CD, de Vries HE. Blood-brain barrier permeability and monocyte infiltration in experimental allergic encephalomyelitis: a quantitative MRI study. Brain 2004;127:616–627. [PubMed: 14691063]

Fukushima, E.; Roeder, SBW. Experimental Pulse NMR. Reading, MA: Addison-Wesley; 1981.

Ge Y, Grossman RI, Udupa JK, Wei L, Mannon LJ, Polansky M, Kolson DL. Brain atrophy in relapsing-remitting multiple sclerosis and secondary progressive multiple sclerosis: longitudinal quantitative analysis. Radiology 2000;214:665–670. [PubMed: 10715027]

Geurts JJ, Barkhof F. Grey matter pathology in multiple sclerosis. Lancet Neurol 2008;7:841–851. [PubMed: 18703006]

Iannucci G, Minicucci L, Rodegher M, Sormani MP, Comi G, Filippi M. Correlations between clinical and MRI involvement in multiple sclerosis: assessment using T(1), T(2) and MT histograms. Journal of the Neurological Sciences 1999;171:121–129. [PubMed: 10581378]

Johnson GA, Benveniste H, Black RD, Hedlund LW, Maronpot RR, Smith BR. Histology by magnetic resonance microscopy. Magn Reson Q 1993;9:1–30. [PubMed: 8512830]

Johnson GA, Cofer GP, Fubara B, Gewalt SL, Hedlund LW, Maronpot RR. Magnetic resonance histology for morphologic phenotyping. Journal of Magnetic Resonance Imaging 2002a;16:423–429. [PubMed: 12353257]

Johnson GA, Cofer GP, Gewalt SL, Hedlund LW. Morphologic phenotyping with MR microscopy: the visible mouse. Radiology 2002b;222:789–793. [PubMed: 11867802]

Kalkers NF, Bergers E, Castelijns JA, van Walderveen MA, Bot JC, Ader HJ, Polman CH, Barkhof F. Optimizing the association between disability and biological markers in MS. Neurology 2001;57:1253–1258. [PubMed: 11591845]

Kochunov P, Lancaster JL, Thompson P, Woods R, Mazziotta J, Hardies J, Fox P. Regional spatial normalization: toward an optimal target. Journal of Computer Assisted Tomography 2001;25:805–816. [PubMed: 11584245]

Kuerten S, Kostova-Bales DA, Frenzel LP, Tigno JT, Tary-Lehmann M, Angelov DN, Lehmann PV. MP4- and MOG:35-55-induced EAE in C57BL/6 mice differentially targets brain, spinal cord and cerebellum. J Neuroimmunol 2007;189:31–40. [PubMed: 17655940]

Kutzelnigg A, Faber-Rod JC, Bauer J, Lucchinetti CF, Sorensen PS, Laursen H, Stadelmann C, Bruck W, Rauschka H, Schmidbauer M, Lassmann H. Widespread demyelination in the cerebellar cortex in multiple sclerosis. Brain Pathol 2007;17:38–44. [PubMed: 17493036]

Lees JR, Golumbek PT, Sim J, Dorsey D, Russell JH. Regional CNS responses to IFN-gamma determine lesion localization patterns during EAE pathogenesis. J Exp Med 2008;205:2633–2642. [PubMed: 18852291]

Liu C, Edwards S, Gong Q, Roberts N, Blumhardt LD. Three dimensional MRI estimates of brain and spinal cord atrophy in multiple sclerosis. Journal of Neurology, Neurosurgery and Psychiatry 1999;66:323–330.

Liu HB, Loo KK, Palaszynski K, Ashouri J, Lubahn DB, Voskuhl RR. Estrogen receptor alpha mediates estrogen's immune protection in autoimmune disease. J Immunol 2003;171:6936–6940. [PubMed: 14662901]

MacKenzie-Graham A, Lee EF, Dinov ID, Bota M, Shattuck DW, Ruffins S, Yuan H, Konstantinidis F, Pitiot A, Ding Y, Hu G, Jacobs RE, Toga AW. A multimodal, multidimensional atlas of the C57BL/6J mouse brain. J Anat 2004;204:93–102. [PubMed: 15032916]

MacKenzie-Graham A, Tinsley MR, Shah KP, Aguilar C, Strickland LV, Boline J, Martin M, Morales L, Shattuck DW, Jacobs RE, Voskuhl RR, Toga AW. Cerebellar cortical atrophy in experimental autoimmune encephalomyelitis. Neuroimage 2006;32:1016–1023. [PubMed: 16806982]

Mauk MD, Medina JF, Nores WL, Ohyama T. Cerebellar function: coordination, learning or timing? Curr Biol 2000;10:R522–R525. [PubMed: 10898992]

Melzer N, Meuth SG, Torres-Salazar D, Bittner S, Zozulya AL, Weidenfeller C, Kotsiari A, Stangel M, Fahlke C, Wiendl H. A beta-lactam antibiotic dampens excitotoxic inflammatory CNS damage in a mouse model of multiple sclerosis. PLoS ONE 2008;3:e3149. [PubMed: 18773080]

Muller DM, Pender MP, Greer JM. Blood-brain barrier disruption and lesion localisation in experimental autoimmune encephalomyelitis with predominant cerebellar and brainstem involvement. J Neuroimmunol 2005;160:162–169. [PubMed: 15710469]

Nicot A, Kurnellas M, Elkabes S. Temporal pattern of plasma membrane calcium ATPase 2 expression in the spinal cord correlates with the course of clinical symptoms in two rodent models of autoimmune encephalomyelitis. Eur J Neurosci 2005;21:2660–2670. [PubMed: 15926914]

Peterson JW, Bo L, Mork S, Chang A, Trapp BD. Transected neurites, apoptotic neurons, and reduced inflammation in cortical multiple sclerosis lesions. Ann Neurol 2001;50:389–400. [PubMed: 11558796]

Pettinelli CB, McFarlin DE. Adoptive transfer of experimental allergic encephalomyelitis in SJL/J mice after in vitro activation of lymph node cells by myelin basic protein: requirement for Lyt 1+ 2- T lymphocytes. J Immunol 1981;127:1420–1423. [PubMed: 6168690]

Rausch M, Hiestand P, Baumann D, Cannet C, Rudin M. MRI-based monitoring of inflammation and tissue damage in acute and chronic relapsing EAE. Magnetic Resonance in Medicine 2003;50:309–314. [PubMed: 12876707]

Renganathan M, Gelderblom M, Black JA, Waxman SG. Expression of Nav1.8 sodium channels perturbs the firing patterns of cerebellar Purkinje cells. Brain Res 2003;959:235–242. [PubMed: 12493611]

Rex DE, Ma JQ, Toga AW. The LONI Pipeline Processing Environment. Neuroimage 2003;19:1033–1048. [PubMed: 12880830]

Rudick RA, Fisher E, Lee JC, Simon J, Jacobs L. Multiple Sclerosis Collaborative Research Group. Use of the brain parenchymal fraction to measure whole brain atrophy in relapsing-remitting MS. Neurology 1999;53:1698–1704. [PubMed: 10563615]

Selvaraj RK, Geiger TL. Mitigation of experimental allergic encephalomyelitis by TGF-beta induced Foxp3+ regulatory T lymphocytes through the induction of anergy and infectious tolerance. J Immunol 2008;180:2830–2838. [PubMed: 18292504]

Shattuck DW, Leahy RM. Automated graph-based analysis and correction of cortical volume topology. IEEE Trans Med Imaging 2001;20:1167–1177. [PubMed: 11700742]

Sled JG, Zijdenbos AP, Evans AC. A nonparametric method for automatic correction of intensity nonuniformity in MRI data. IEEE Trans Med Imaging 1998;17:87–97. [PubMed: 9617910]

Stevenson VL, Miller DH, Leary SM, Rovaris M, Barkhof F, Brochet B, Dousset V, Filippi M, Hintzen R, Montalban X, Polman CH, Rovira A, de Sa J, Thompson AJ. One year follow up study of primary and transitional progressive multiple sclerosis. Journal of Neurology, Neurosurgery and Psychiatry 2000;68:713–718.

Suen WE, Bergman CM, Hjelmstrom P, Ruddle NH. A critical role for lymphotoxin in experimental allergic encephalomyelitis. J Exp Med 1997;186:1233–1240. [PubMed: 9334362]

Tonra JR. Cerebellar susceptibility to experimental autoimmune encephalomyelitis in SJL/J mice: potential interaction of immunology with vascular anatomy. Cerebellum 2002;1:57–68. [PubMed: 12879974]

Tonra JR, Reiseter BS, Kolbeck R, Nagashima K, Robertson R, Keyt B, Lindsay RM. Comparison of the timing of acute blood-brain barrier breakdown to rabbit immunoglobulin G in the cerebellum and spinal cord of mice with experimental autoimmune encephalomyelitis. J Comp Neurol 2001;430:131–144. [PubMed: 11135250]

Trapp BD, Peterson J, Ransohoff RM, Rudick R, Mork S, Bo L. Axonal transection in the lesions of multiple sclerosis. N Engl J Med 1998;338:278–285. [PubMed: 9445407]

Trapp BD, Ransohoff R, Rudick R. Axonal pathology in multiple sclerosis: relationship to neurologic disability. Curr Opin Neurol 1999;12:295–302. [PubMed: 10499174]

Uemura Y, Ohno H, Ohzeki Y, Takanashi H, Murooka H, Kubo K, Serizawa I. The selective M-CSF receptor tyrosine kinase inhibitor Ki20227 suppresses experimental autoimmune encephalomyelitis. J Neuroimmunol 2008;195:73–80. [PubMed: 18378004]

Wang L, Wang R, Herrup K. E2F1 works as a cell cycle suppressor in mature neurons. Journal of Neuroscience 2007;27:12555–12564. [PubMed: 18003834]

Waxman SG. Cerebellar dysfunction in multiple sclerosis: evidence for an acquired channelopathy. Prog Brain Res 2005;148:353–365. [PubMed: 15661203]

Weinshenker BG, Issa M, Baskerville J. Long-term and short-term outcome of multiple sclerosis: a 3-year follow-up study. Arch Neurol 1996;53:353–358. [PubMed: 8929158]

Woods RP, Grafton ST, Holmes CJ, Cherry SR, Mazziotta JC. Automated image registration: I. General methods and intrasubject, intramodality validation. Journal of Computer Assisted Tomography 1998a;V22:139–152.

Woods RP, Grafton ST, Watson JD, Sicotte NL, Mazziotta JC. Automated image registration: II. Intersubject validation of linear and nonlinear models. Journal of Computer Assisted Tomography 1998b;22:153–165. [PubMed: 9448780]
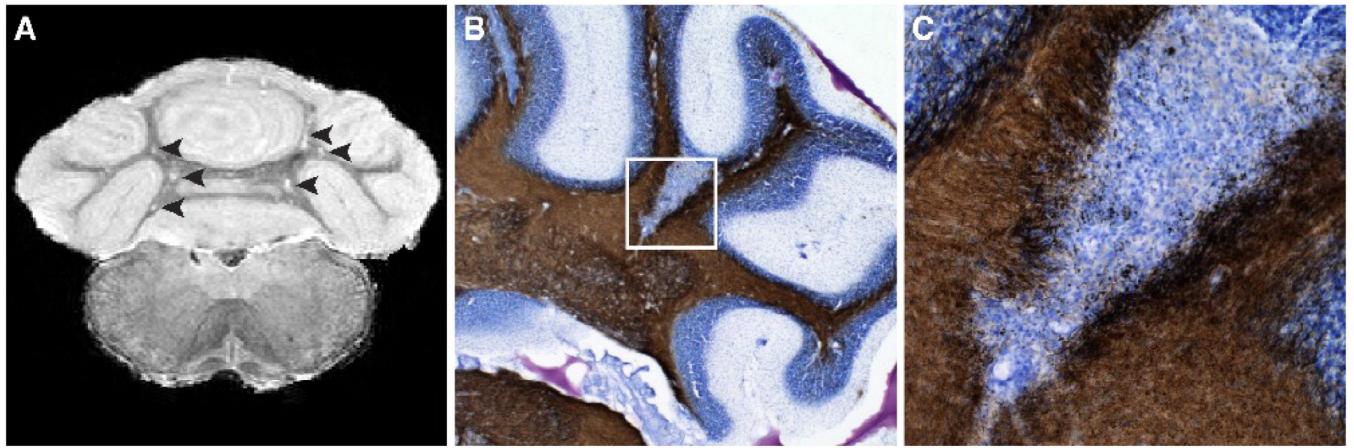
Fig. 1. White Matter Lesions in EAE
A, Postmortem high-resolution T2-weighted magnetic resonance microscopy image of a C57BL/6 mouse with myelin oligodendrocyte glycoprotein-induced active experimental autoimmune encephalomyelitis (EAE). Cerebellar white matter lesions are clearly visible as T2 hyperintensities (arrowheads) in the early stages of disease (day 15). *B,* A 2X magnification image of a serial section though the cerebellum of a mouse with EAE (day 55) stained with a reducing silver myelin stain and counterstained with thionin (Nissl). The focal lesions are clearly visible as disruptions in the cerebellar white matter (stained light brown). *C,* A 10X magnification image of the inset in panel B demonstrating a typical lesion.
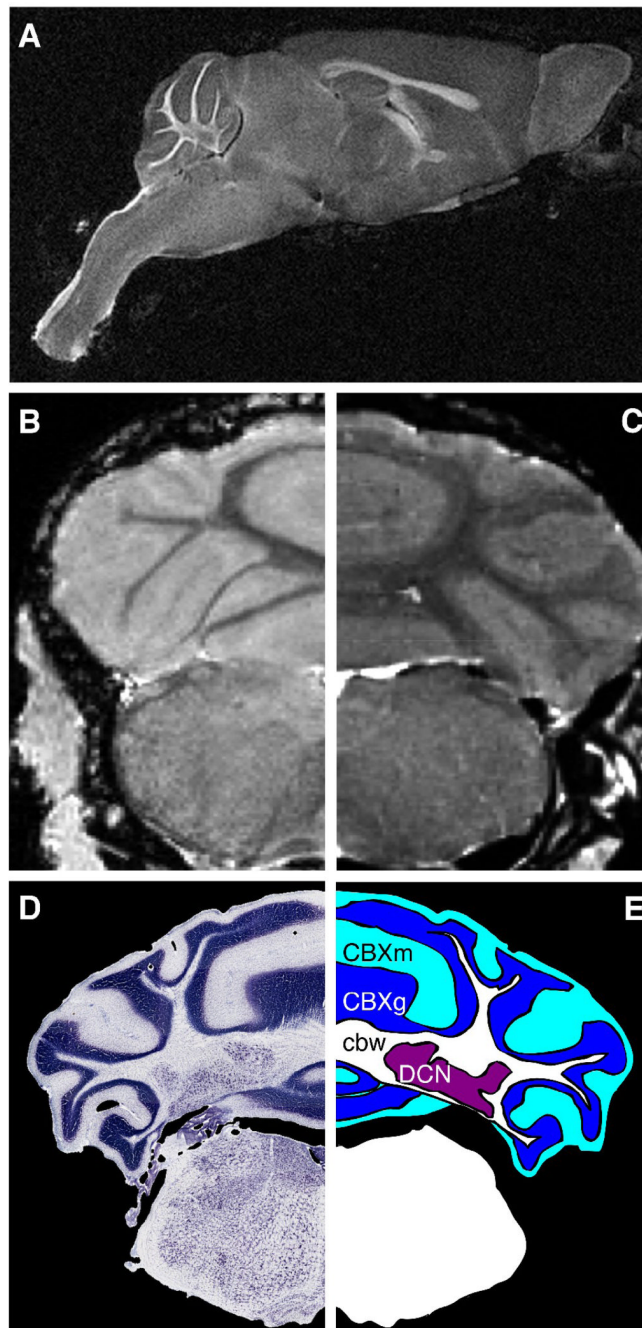
Fig. 2. Mouse Brain Imaging
A, A diffusion weighted image of a 100 day-old normal mouse brain demonstrating the paucity of white matter in the mouse brain. *B,* A magnetic resonance microscopy (MRM) image of the cerebellum of a normal control C57BL/6J mouse brain. *C,* A magnetic resonance histology (MRH) image of the cerebellum of a normal control C57BL/6J mouse brain. The qualitatively different contrast allows us to unambiguously delineate the molecular layer of the cerebellum. *D,* A Nissl-stained section of tissue through the cerebellum of a 100 day-old normal mouse. *E,* An anatomical delineation derived from the Nissl-stained image highlighting the different layers of the cerebellar cortex. Cerebellar white matter (cbw); granule cell layer of the

cerebellar cortex (CBXg); molecular layer of the cerebellar cortex (CBXm); deep cerebellar nuclei (DCN).
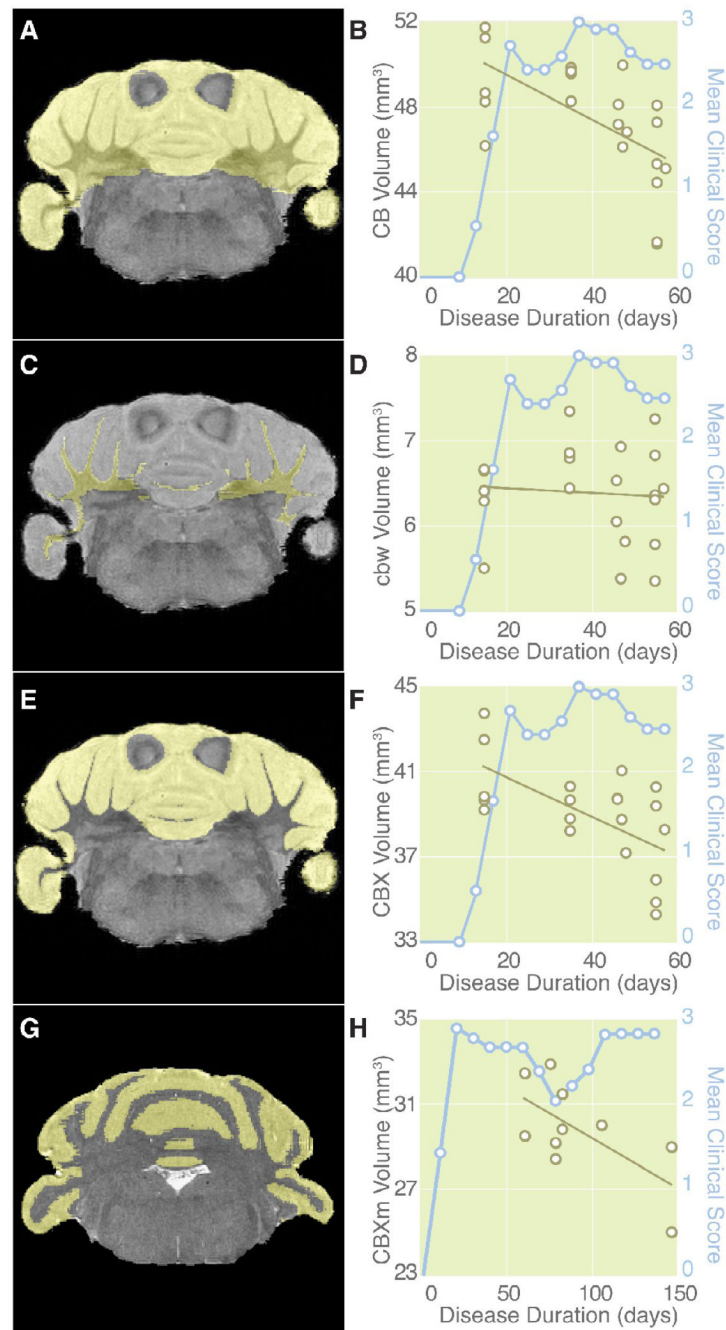
Fig. 3. Gray Matter Atrophy in the Cerebella of Mice with EAE
A, Magnetic resonance microscopy image of the brain of a mouse with EAE with the delineation of the cerebellum overlaid in yellow. *B,* Dot plot of the cerebellum (CB) volume plotted against disease duration demonstrated an inverse correlation (R = −0.6178, n = 21, p = 0.0028). The disease course for this cohort of mice is overlaid on the graph for illustrative purposes. *C,* Magnetic resonance microscopy image of the brain of a mouse with EAE with the delineation of the cerebellar white matter overlaid in yellow. *D,* Dot plot of the cerebellar white matter (cbw) volume plotted against disease duration did not demonstrate a significant correlation (R = −0.0747, n = 21, p = 0.75). The disease course for this cohort of mice is overlaid on the graph for illustrative purposes. *E,* Magnetic resonance microscopy image of the brain

of a mouse with EAE with the delineation of the cerebellar cortex overlaid in yellow. *F,* Dot plot of the cerebellar cortex (CBX) volume plotted against disease duration demonstrated an inverse correlation (R = −0.6207, n = 21, p = 0.0027). The disease course for this cohort of mice is overlaid on the graph for illustrative purposes. *G,* Magnetic resonance histology image of the brain of a mouse with EAE with the delineation of the molecular layer of the cerebellar cortex overlaid in yellow. *H,* Dot plot of the molecular layer of the cerebellar cortex (CBXm) volume plotted against disease duration demonstrated an inverse correlation (R = −0.6562, n = 10, p = 0.039). The disease course for this cohort of mice is overlaid on the graph for illustrative purposes.
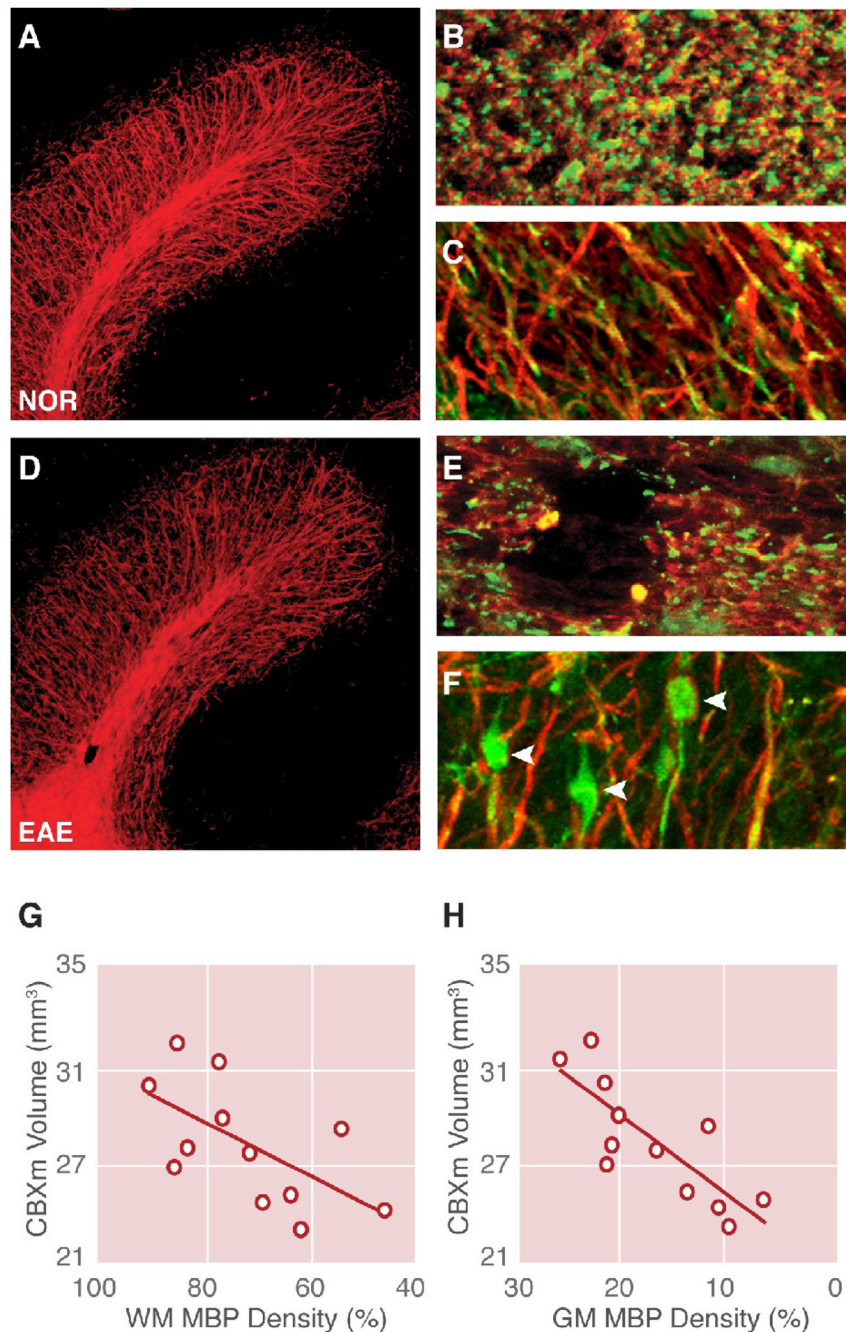
Fig. 4. Demyelination in the Cerebella of Mice with EAE
A, MBP immunostained confocal image at 10X magnification in the cerebellum of a normal control mouse. *B,* MBP (red)/NF200 (green) double-stained confocal image at 60X magnification demonstrating normal morphology in the cerebellar white matter. *C,* MBP/ NF200 double-stained confocal image at 60X magnification demonstrating normal morphology in the granule cell layer of the cerebellar cortex. *D,* MBP stained confocal image at 10X magnification in the cerebellum of a mouse with EAE (day 63). *E,* MBP/NF200 double-stained confocal image at 60X magnification demonstrating a lesion devoid of myelin or axons in the cerebellar white matter. *F,* MBP/NF200 double-stained confocal image at 60X magnification demonstrating swollen axons and axon retraction bulbs in the granule cell layer

of the cerebellar cortex (arrowheads). *G,* Dot plot of the molecular layer of the cerebellar cortex (CBXm) volume plotted against MBP staining density in the cerebellar white matter demonstrated a direct correlation ($R = 0.6132$, $n = 12$, $p = 0.03398$). *H,* Dot plot of the molecular layer of the cerebellar cortex (CBXm) volume plotted against MBP staining density in the cerebellar cortex demonstrated a direct positive correlation ($R = 0.8069$, $n = 12$, $p = 0.001514$).
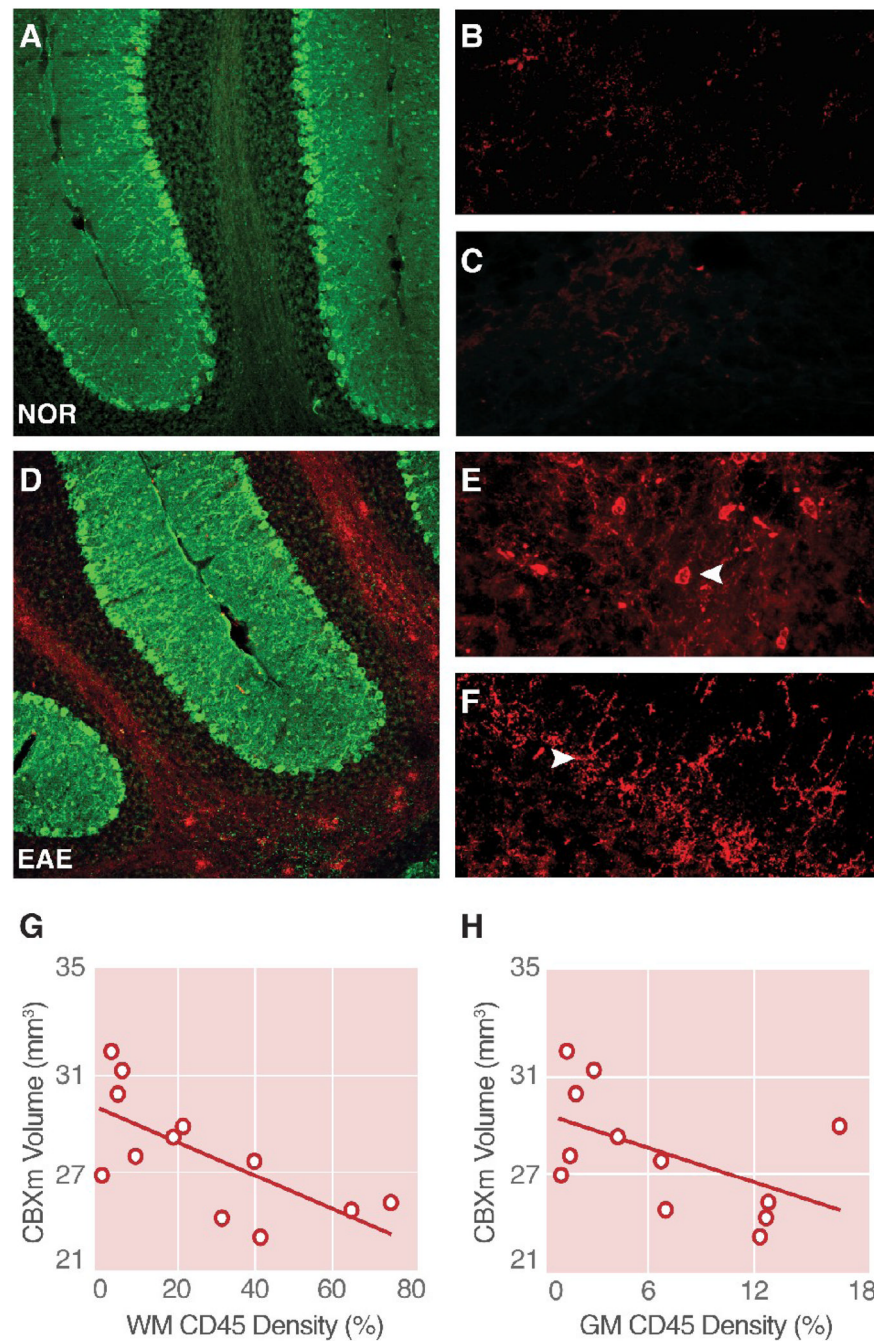
Fig. 5. Inflammation in the Cerebella of Mice with EAE
A, CD45 (red)/parvalbumin (green) double-stained confocal image at 10X magnification in the cerebellum of a normal control mouse. *B,* CD45 immunostained confocal image at 63X magnification demonstrating minimal CD45 staining in the cerebellar white matter (green channel removed for clarity). *C,* CD45 immunostained confocal image at 63X magnification demonstrating a minimal CD45 staining in the molecular layer of the cerebellar cortex (green channel removed for clarity). *D,* CD45/parvalbumin double-stained confocal image at 10X magnification in the cerebellum of a mouse with EAE (day 70). *E,* CD45 immunostained confocal image at 63X magnification demonstrating a CD45$^+$ cell with a macrophage-like morphology in the cerebellar white matter (arrowhead) (green channel removed for clarity).

F, CD45 immunostained confocal image at 63X magnification demonstrating a CD45+ cell with a microglia-like morphology in the molecular layer of the cerebellar cortex (arrowhead) (green channel removed for clarity). *G,* Dot plot of the molecular layer of the cerebellar cortex (CBXm) volume plotted against CD45 staining density in the cerebellar white matter demonstrated an inverse correlation (R = −0.6942, n = 12, p = 0.01226). *H,* Dot plot of the molecular layer of the cerebellar cortex volume plotted against CD45 staining density in the cerebellar cortex demonstrated an inverse correlation that did not reach statistical significance (R = −0.5345, n = 12, p = 0.07338).
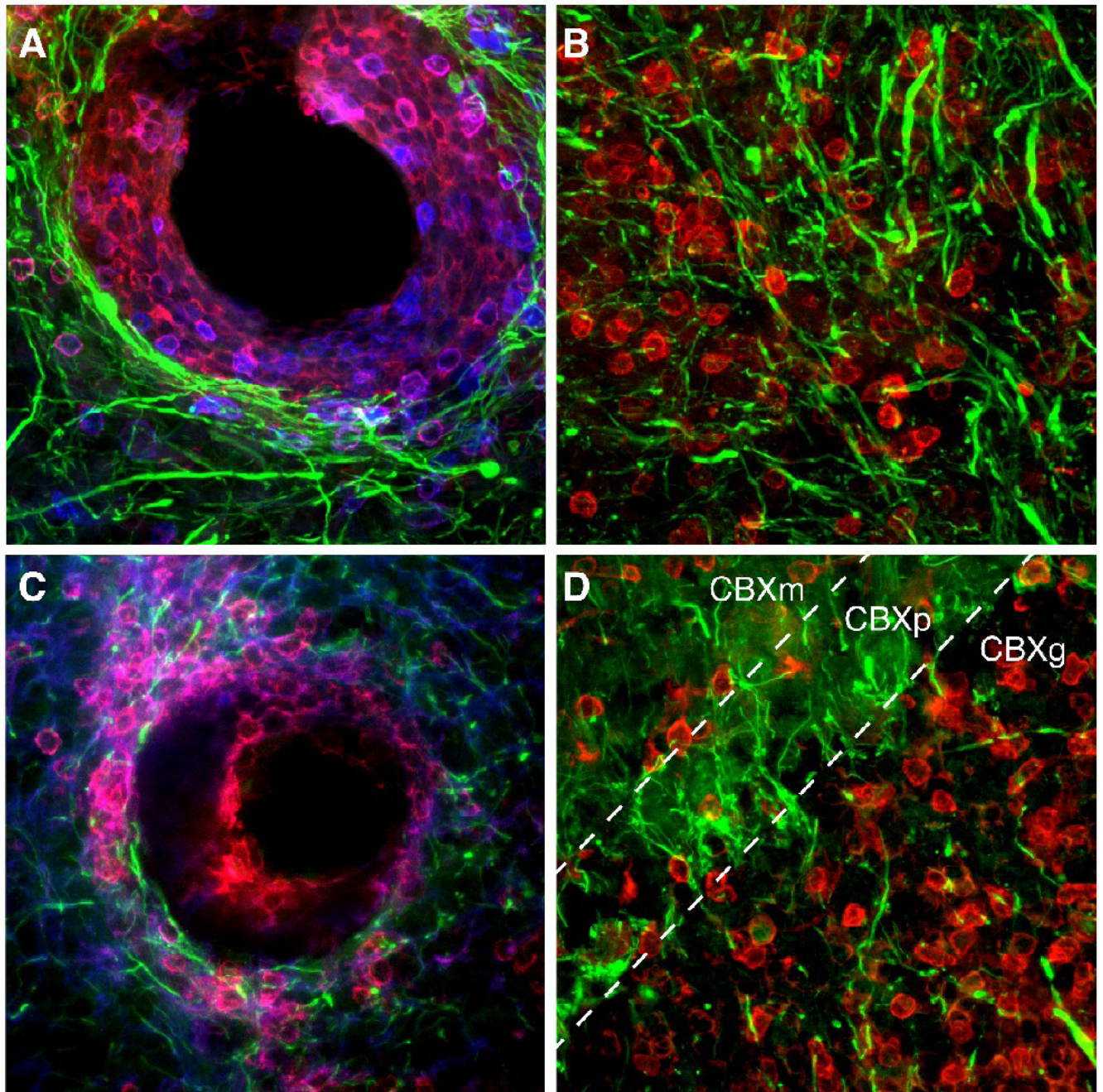
Fig. 6. Characterization of CD45$^+$ cells in the Cerebella of Mice with EAE
A, CD3 (red)/NF200 (green)/CD45 (blue) triple-stained confocal image at 40X magnification focusing on a lesion near a blood vessel in the white matter of the cerebellum of a mouse with EAE (day 55). *B,* CD3 (red)/NF200 (green) double-stained confocal image at 40X magnification focusing on cellular infiltration in the granule cell layer of the cerebellar cortex of a mouse with EAE (day 55). *C,* Mac-3 (red)/NF200 (green)/CD45 (blue) triple-stained confocal image at 40X magnification focusing on a lesion near a blood vessel in the white matter of the cerebellum of a mouse with EAE (day 55). *D,* Mac-3 (red)/NF200 (green) double-stained confocal image at 40X magnification focusing on cellular infiltration in the cerebellar cortex of a mouse with EAE (day 55). Dashed lines indicate the layers of the cerebellar cortex.

Granule cell layer of the cerebellar cortex (CBXg); molecular layer of the cerebellar cortex (CBXm); Purkinje cell layer of the cerebellar cortex (CBXp).
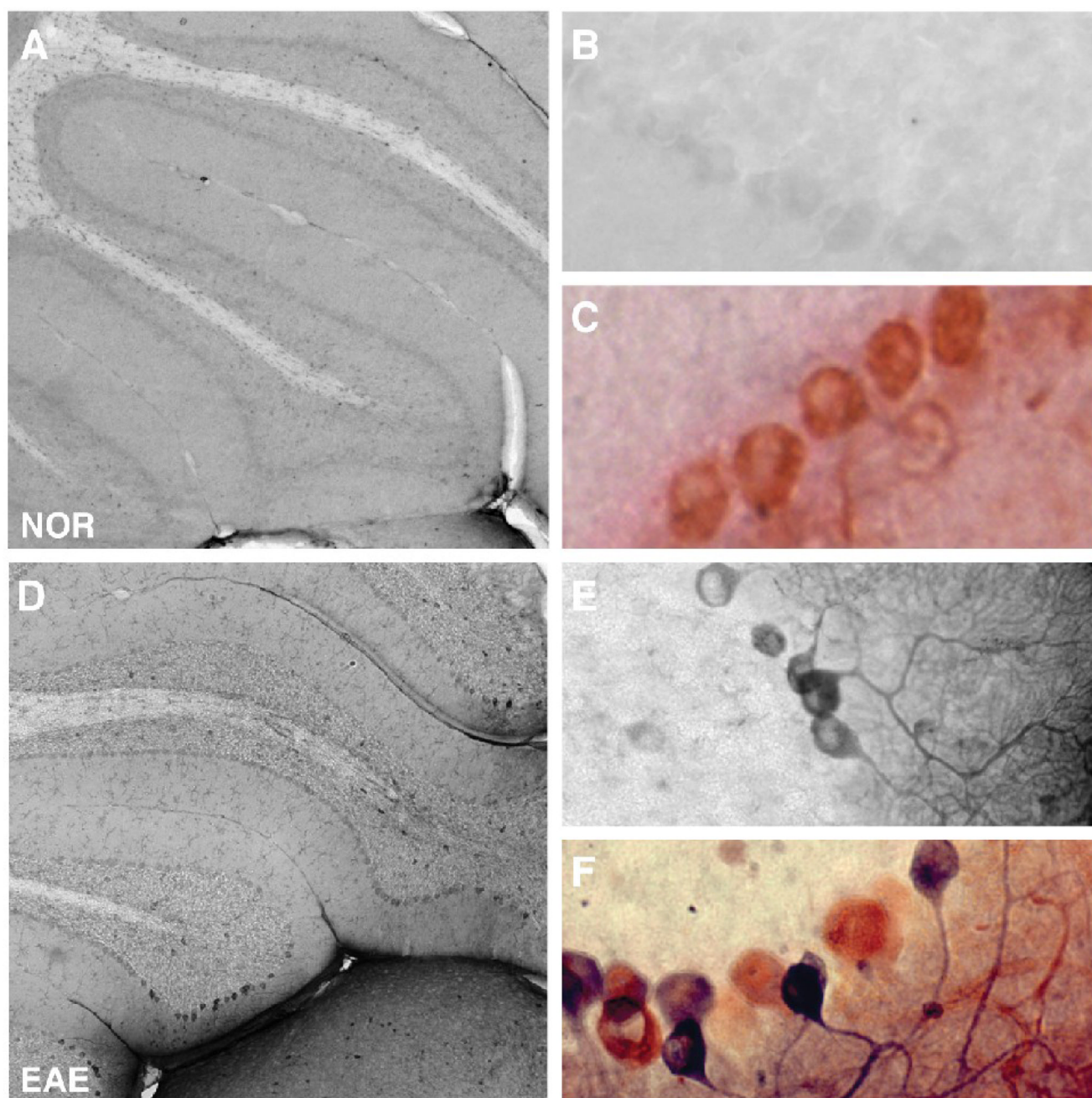
Fig. 7. Apoptosis in the Cerebella of Mice with EAE
A, Caspase-3 immunostained light microscopy images at 10X magnification in the cerebellum of a normal control mouse. *B,* Caspase-3 immunostained light microscopy images at 40X magnification demonstrating minimal caspase-3 staining. *C,* Caspase-3 (black)/calbindin-2 (red) double-stained light microscopy images at 40X magnification demonstrating normal morphology in the cerebellar cortex. *D,* Caspase-3 immunostained light microscopy images at 10X magnification in the cerebellum of a mouse with EAE (day 63). *E,* Caspase-3 immunostained light microscopy images at 40X magnification demonstrating caspase-3^{+} cells with Purkinje cell-like morphology in the Purkinje layer of the cerebellar cortex. *F,* Caspase-3/

calbindin-2 double-stained light microscopy images at 40X magnification demonstrating calbindin-2$^+$ Purkinje cells undergoing caspase-3 mediated apoptosis.
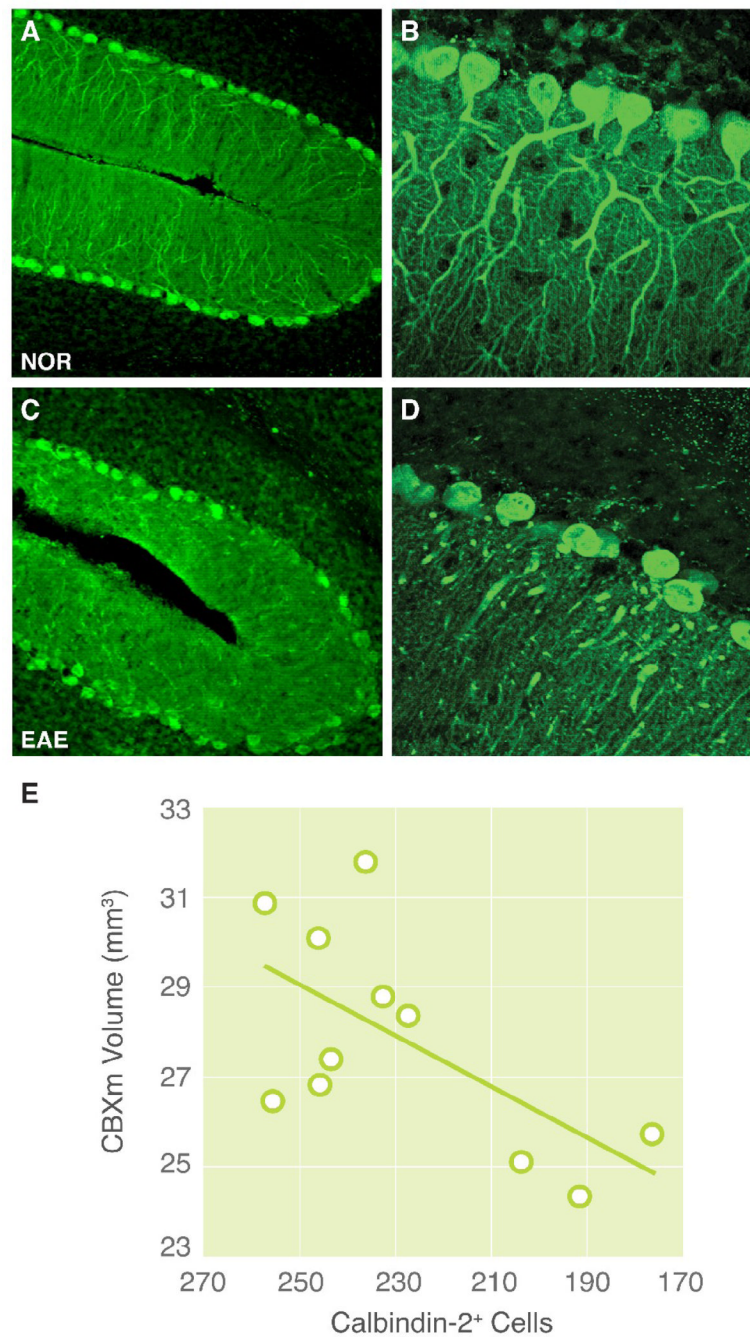
Fig. 8. Purkinje Cells in the Cerebella of Mice with EAE
A, Calbindin-2 stained confocal images at 10X magnification in the cerebellum of a normal control mouse. *B,* Calbindin-2 immunostained confocal images at 40X magnification demonstrating normal morphology in the Purkinje layer of the cerebellar cortex. *C,* Calbindin-2 stained confocal images at 10X magnification in the cerebellum of a mouse with EAE (day 70). *D,* Calbindin-2 immunostained images at 40X magnification demonstrating a decrease in Purkinje cell number, changes in their dendritic arborization, and a general loss in the organization of the Purkinje layer of the cerebellar cortex. *E,* Dot plot of the molecular layer of the cerebellar cortex volume (CBXm) plotted against the number of calbindin-2+ Purkinje

cells demonstrated a direct correlation (R = 0.6287, n = 11, p = 0.03826). Cell counts for this study focused on lobule I/II and III.
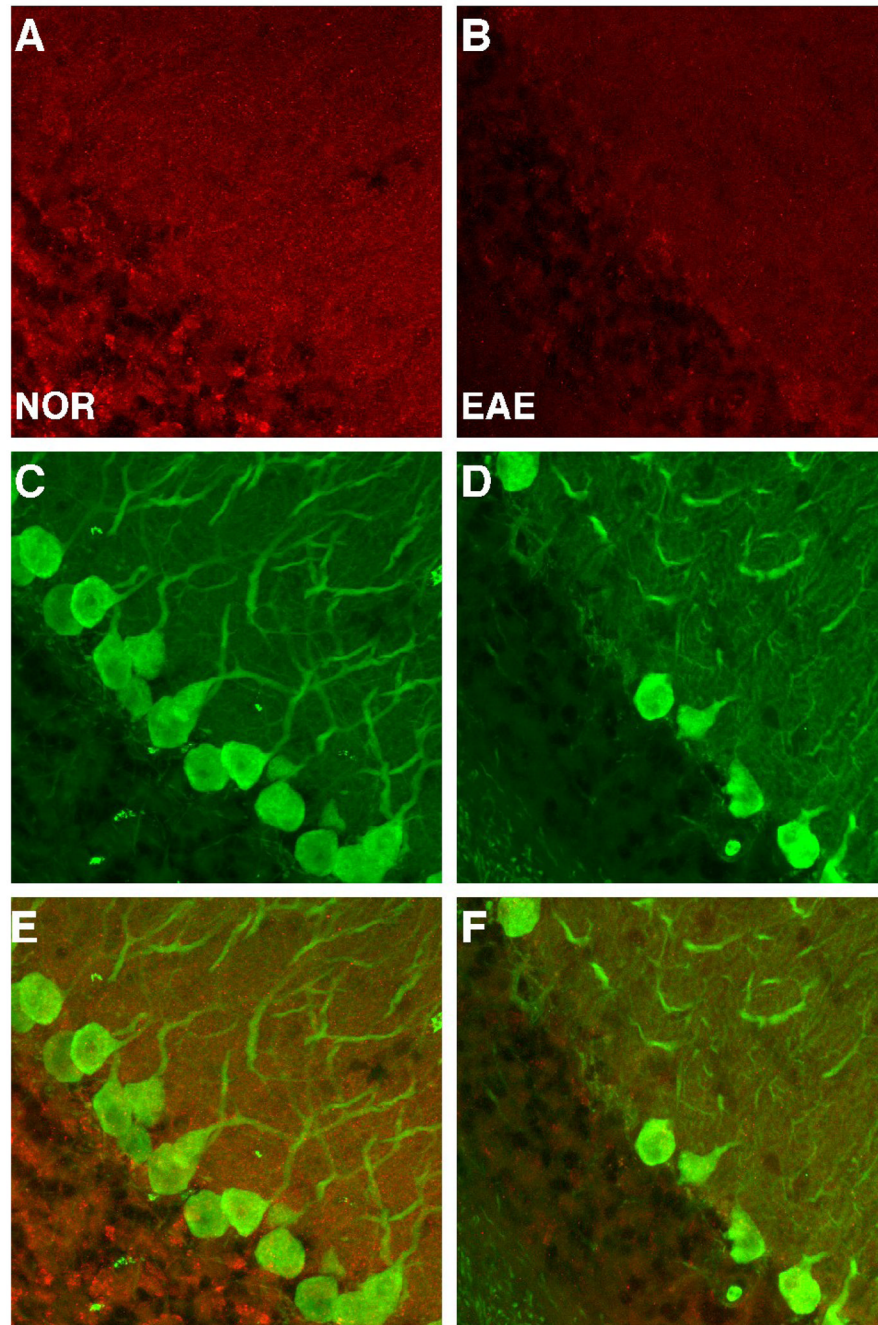
Fig. 9. Synapsin is Decreased in the Cerebella of Mice with EAE
A, Synapsin stained confocal image at 40X magnification of the of the cerebellar cortex of a normal control mouse. *B,* Synapsin stained confocal image at 40X magnification of the cerebellar cortex of a mouse with EAE (day 55). *C,* Calbindin-2 stained confocal image at 40X magnification of the cerebellar cortex of a normal control mouse. *D,* Calbindin-2 stained confocal image at 40X magnification of the cerebellar cortex of a mouse with EAE (day 55). *E,* Merge of synapsin (red)/calbindin-2 (green) double-stained confocal image at 40X magnification of the cerebellar cortex of a normal control mouse. *F,* Merge of synapsin/calbindin-2 double-stained confocal image at 40X magnification of the cerebellar cortex of a mouse with EAE (day 55).
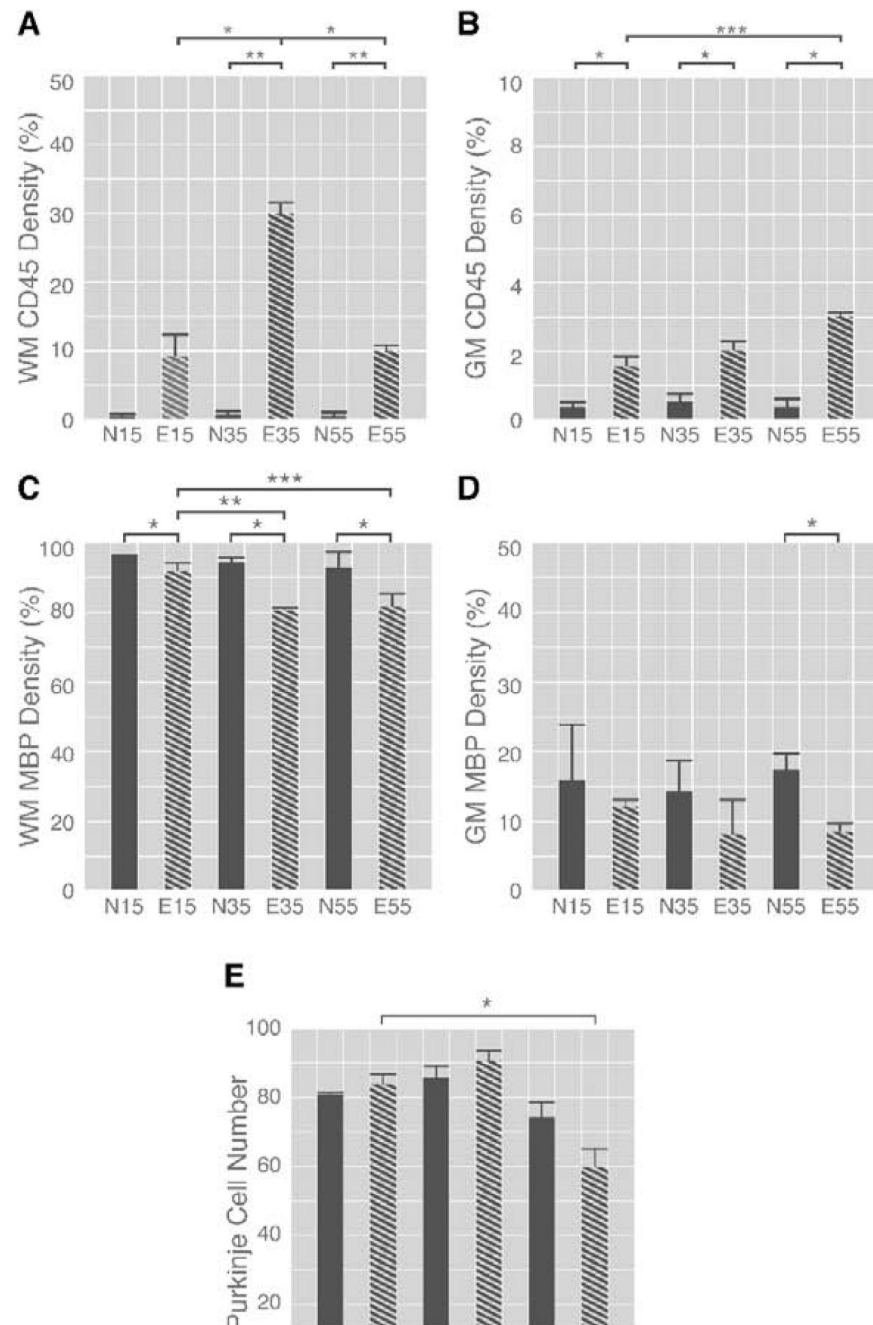
Fig. 10. Time Course of Pathology in the Cerebella of Mice with EAE
A, Mean values and SEM of white matter CD45 staining density for control or EAE mice at each time point. *B,* Mean values and SEM of gray matter CD45 staining density for control or EAE mice at each time point. *C,* Mean values and SEM of white matter myelin basic protein staining density for control or EAE mice at each time point. *D,* Mean values and SEM of gray matter myelin basic protein staining density for control or EAE mice at each time point. *E,* Mean values and SEM of Purkinje cell number for control or EAE mice at each time point. Cell counts for this study focused on lobule I/II. The letter E indicates mice with EAE and the letter N indicates normal, age-matched controls. The number following the letter indicates the number of days post-induction. Asterisks indicate significance (* p < 0.05, ** p < 0.01, *** p

< 0.005). All differences which are significant at p > 0.01 (two asterisks or more) survive the application of the Bonferroni correction for post hoc testing.